Supplementary Materials for

Giant Transverse Thermoelectric Effect Induced by Topological Transition in Polycrystalline Dirac Semimetal Mg_3Bi_2

Tao Feng[1]†, Panshuo Wang[2]†, Zhijia Han[1], Liang Zhou[2], Wenqing Zhang[1]*, Qihang Liu[2]*, Weishu Liu[1]*

[1] Department of Materials Science and Engineering, Southern University of Science and Technology, Shenzhen 518055, China

[2] Department of Physics and Shenzhen Institute for Quantum Science & Engineering, Southern University of Science and Technology, Shenzhen 518055, China

*Correspondence to: liuws@sustech.edu.cn, liuqh@sustech.edu.cn, zhangwq@sustech.edu.cn

MATERIALS AND METHODS

Sample preparation

The Mn-doped Mg_3Bi_2 samples were synthesized through a combined approach of mechanical alloying and spark plasma sintering (SPS). Magnesium turnings (Mg, 99.98%, Acros Organics), bismuth shots (Bi, 99.999%, 5N Plus) and Manganese powders (Mn, 99.95%, Alfa Aesar) were weighed according to the composition of $Mg_{3.4}Bi_2Mn_x$ ($0 \leq x \leq 0.15$), and were loaded into a stainless-steel ball milling jar in a glove box under an Ar atmosphere with an oxygen level of <1 ppm. After ball milling for 8 hours in a SPEX 8000M mixer, the ball-milled powders were loaded into a graphite die with an inner diameter of 12.7 mm, in the glove box. The graphite die with the loading powder was immediately sintered at 700°C under a pressure of 50 MPa for 5 min via spark plasma sintering (SPS) (SPS-211Lx, Fuji Electronic Industrial Co. LTD). The SPS bulks were ~12.7 mm in diameter, with a thickness of ~8 mm.

Sample characterization

The phase purity of the product was measured by powder X-ray diffraction (XRD) on a Rigaku D/Max-2550 instrument (Cu Kα radiation, $\lambda = 1.5418$ Å, 18 KW). The temperature-dependent thermal conductivity was measured adiabatically using the thermal transport option (TTO) on a Quantum Design Physical Property Measurement System (PPMS 14 Tesla) with one-heater and two-thermometer configuration. With the same option, the transverse and longitudinal thermopower were simultaneously measured adiabatically. We mounted the sample with transverse voltage leads, which were purposefully offset by a distance X from each other so that the longitudinal (Seebeck) and transverse (Nernst) voltage could both be measured. The heat flowed from left to right, and the thermometers T-hot and T-cold were mounted on the left and right leads located on the lower side of the sample. The V+ and V– leads measured the diagonal voltage component, and by measuring it as a function of the magnetic field in both the positive and negative fields, we could employ symmetry arguments to separate the longitudinal thermopower from the

transverse thermopower. The longitudinal and Hall resistivities were measured using the electronic transport option (ETO) in PPMS using the standard four-probe method.

Usually, three possible defects in the Mn-doped Mg_3Bi_2 are considered, including (i) Mg tetrahedron-site (1/3, 2/3, 0.631) with 4 Sb-neighbors, (ii) Mg octahedron-site (0,0,0) with six Sb-neighbors and (iii) interstitial positions (2/3, 1/3, 0.182) with 4 Mg-neighbor. According to the formation energy calculations (Figure S3), Mn prefers occupying the Mg-tetrahedral site (black lines in Figure S3). By using the defect of $Mn_{Mg\text{-}tet}$, the Rietveld refinements of XRD were conducted using GSAS software with the trigonal lattice geometry of the space group $P\bar{3}m1$. The refined parameters Chi2 are 5.721, 6.652, 5.859, 6.831, 6.773, 5.731 for x = 0, 0.025, 0.075, 0.1, 0.125, and 0.15, respectively, in $Mg_{3+\delta}Bi_2$:Mn_x. The detailed refined crystallographic parameters of the obtained $Mg_{3+\delta}Bi_2$:Mn_x sample are list is Table S2-S7.

Calculation methods

Electronic structure calculations were based on the density functional theory (DFT) plus the on-site repulsion (U) method [1] implemented in the Vienna ab initio simulation package (VASP) [2,3], where the exchange-correlation potential was treated by generalized gradient approximation (GGA) of the Perdew−Burke−Ernzerhof (PBE) functional [4] and the ionic potential was based on the projector augmented wave (PAW) method [5,6]. Owing to the strong relativistic effect in Bismuth, spin-orbit coupling (SOC) was also considered for the energy band dispersion calculations. The energy cutoff of the plane wave was set to 600 eV. The on-site Coulomb repulsion U and exchange parameter J were set to be 3 and 0 eV, respectively, for Mn 3d orbital. For Brillouin zone sampling, a $19 \times 19 \times 9$ Gamma centered K-point mesh was used for the 5-atom Mg_3Bi_2 unit cell for the original and strained structure calculations. The convergence criteria of the energy and force were set to $10^{-6}\,eV$ and 0.001 eVÅ^{-1}, respectively. A $7 \times 7 \times 13$ Gamma centered K-point mesh was used for the $3 \times 3 \times 1$ supercell for the Mn doping Mg_3Bi_2

calculations, and the corresponding convergence criteria of the energy and force were set to $10^{-6}\,eV$ and 0.01 eVÅ^{-1}, respectively. The tight-binding model Hamiltonian adapted for the Wannier interpolation implemented in the WannierTools package [7,8] (i.e., electrical conductivity calculation) was constructed by the Wannier90 software [9] using the maximally localized Wannier function approach [10-12]. The s, p orbits of Mg, p orbits of Bi and s, d orbits of Mn were selected as the initial projectors for Wannier90 software. The irreducible representations and parities for high symmetric $\vec{k}$ points and lines of electronic states of original and strained Mg_3Bi_2 were analyzed through the open-source program Irvsp [13].

For Fig. 3E and 3F in the main text, we adopt the supercell method (i.e. one Mn_{Mg} defect in a supercell) to simulate the translational symmetry breaking, and fully relax all the atoms to process the distortions induced by Mn doping. Then we use the "effective band structure" (EBS) method to unfold the E-k dispersion of the relaxed supercell with Mn doping into the spectrum density in the pristine BZ, capturing the disorder effect influencing the band structure. Energy band broadening effects are observed in this approach (see Fig. 3E and 3F).

The formation energies of Mn with respect to the chemical potential of Mg (μ_{Mg}) and Mn (μ_{Mn}) are calculated, including the tetrahedral site of Mg ($Mn_{Mg\text{-}tet}$), octahedral site of Mg ($Mn_{Mg\text{-}oct}$), and interstitial site (I_{Mn}). As shown in Figure S14, Mn prefers occupying the tetrahedral site of Mg (black line). The formation energies of the defect I_{Mn} are much larger than the other two types of point defects, i.e., $Mn_{Mg\text{-}tet}$ and $Mn_{Mg\text{-}oct}$ in the Mg_3Bi_2.

Transport calculation methods

Generally the magnetoresistance (MR) can be expressed as:

$$MR = \frac{\rho(B) - \rho(0)}{\rho(0)} \times 100\%, \tag{S1}$$

where $\rho(B)$ is the electrical resistivity. $\rho(B)$ is a function of the external magnetic field B, and it is the inverse of the electrical conductivity tensor σ, that is:

$$\rho = \sigma^{-1}. \tag{S2}$$

With the relaxation time approximation and the Boltzmann equation, taking into account the uniform magnetic field, the electrical conductivity tensor was formulated as:

$$\sigma = \sum_n \sigma^{(n)} = \sum_n \frac{e^2}{4\pi^3} \int dk \tau[\epsilon_n(k)] v_n(k) \bar{v}_n(k) \left(-\frac{\partial f}{\partial \epsilon} \right)_{\epsilon = \epsilon_n(k)}, \tag{S3}$$

where e is the element charge, $\epsilon_n(k)$ is the nth band energy at the k point in the Brillouin zone with the corresponding relaxation time $\tau[\epsilon_n(k)]$, f is the Fermi distribution function of equilibrium state, $v_n(k)$ is the Fermi velocity, and $\bar{v}_n(k)$ is a weighted average of the velocity over the past history of the electron orbit passing through k:

$$\bar{v}_n(k) = \int_{-\infty}^{0} \frac{dt}{\tau_n} e^{\frac{t}{\tau_n}} v_n(k(t)). \tag{S4}$$

The time evolution of the wave vector k followed:

$$\frac{dk_n(t)}{dt} = -\frac{e}{\hbar} v_n(k(t)) \times B. \tag{S5}$$

Positive relationship between S and ρ

Without loss of generality, we consider a case where the temperature gradient is along the x direction (i.e., $\nabla_x T \neq 0$, $\nabla_y T = \nabla_z T = 0$), and the magnetic field B is along the z direction. The transverse thermopower S_{xy} can be expressed as:

$$S_{xy} = \frac{E_y}{|-\nabla_x T|} = \frac{\sigma_{xy}\alpha_{xx} + \sigma_{xx}\alpha_{yx}}{\sigma_{xx}\sigma_{yy} + \sigma_{xy}^2}, \tag{S6}$$

where S, E, α, and σ are thermopower, electric field, thermoconductivity tensor and electrical conductivity, respectively, with the subscripts (x, y) indicating the corresponding directions. Generally, the transverse electrical conductivity σ_{xy} is

several orders of magnitude smaller than the longitudinal terms σ_{xx} and σ_{yy}. Thus, the transverse thermopower S_{xy} can be approximately simplified as:

$$S_{xy} \approx \alpha_{yx}/\sigma_{yy} \approx \alpha_{yx} \cdot \rho_{yy}, \tag{S7}$$

where ρ is the electrical resistivity.

Relaxation time approximation

Due to the general linear relationship of carrier mobility and relaxation time:

$$\mu = \frac{e\tau}{m^*}, \tag{S8}$$

where μ, e, τ and m^* are carrier mobility, elementary charge, relaxation time and effective mass, respectively, a longer relaxation time is expected. And the maximum $B\tau$ here is set to $40(T \cdot ps)$.

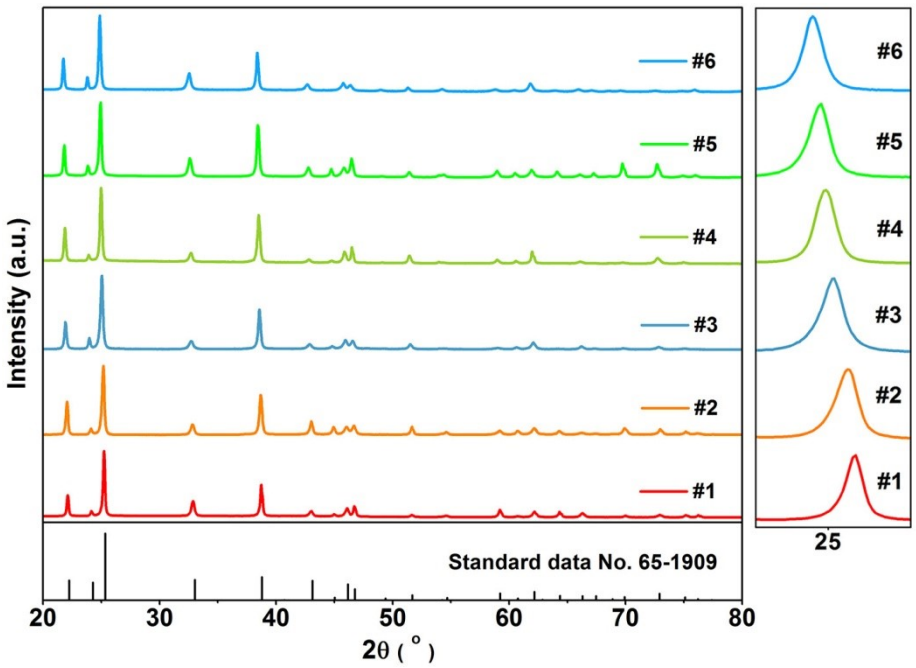

Fig. S1. XRD patterns of the obtained $Mg_{3+\delta}Bi_2$:Mn_x materials recorded at room temperature. The diffraction peaks of all the samples are well matched with the standard data of trigonal Mg_3Bi_2 (JCPDS No. 65-1909). The inset figure is the relative positions of (101) peak of $Mg_{3+\delta}Bi_2$:Mn_x, which gradually shifts to a lower degree with the increase of Mn content, indicating an increased cell parameters according to the Bragg equation.

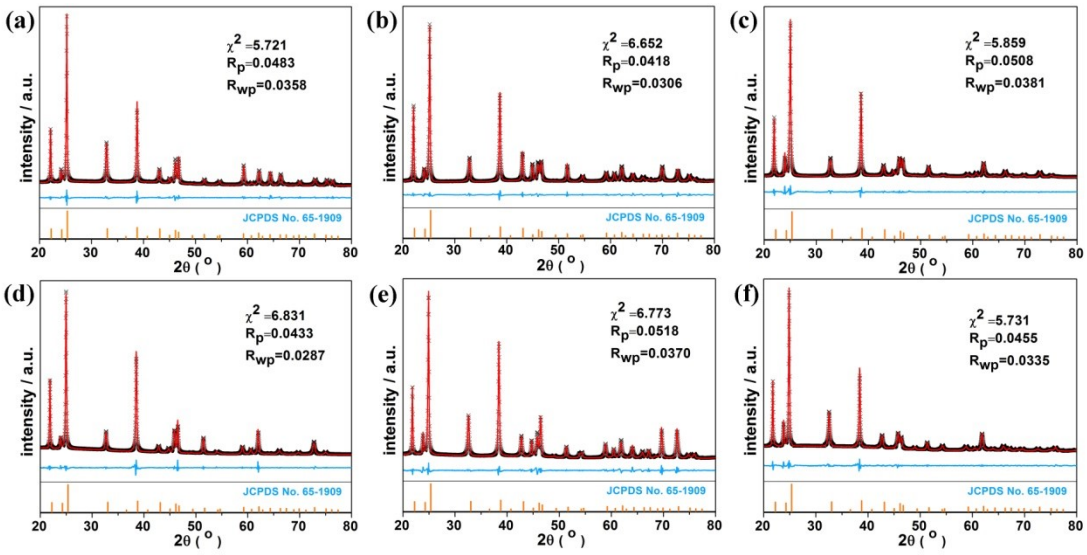

Fig. S2. Rietveld refinement XRD patterns of $Mg_{3+\delta}Bi_2$:Mn_x with (a) x=0, (b) x=0.025, (c) x=0.075, (d) x=0.1, (e) x=0.125, and (f) x=0.15 based on the trigonal lattice geometry of the space group $P\bar{3}m1$.

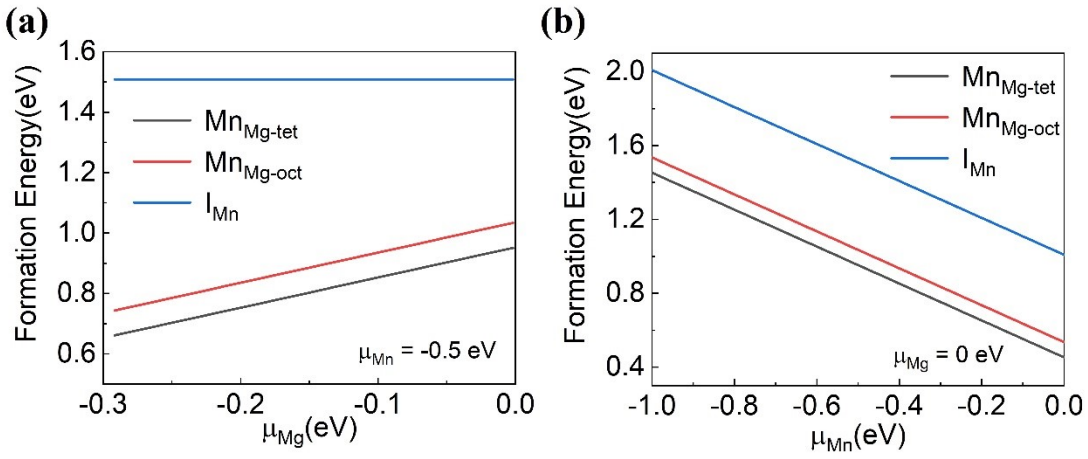

Fig. S3. Formation energies of Mn occupying the tetrahedral site of Mg (black line), octahedral site of Mg (red line), and interstitial site (blue line) with respect to the chemical potendital of (a) Mg and (b) Mn.

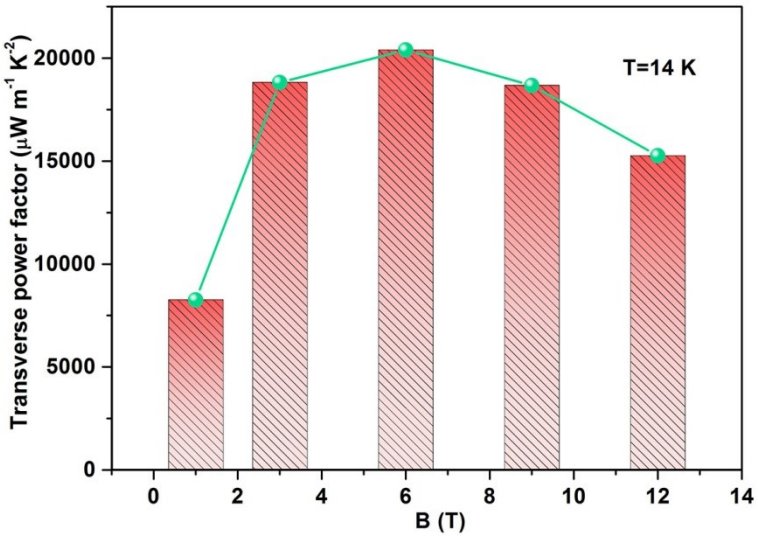

Fig. S4. Transverse power factor of Mn-doped $Mg_{3+\delta}Bi_2$ sample with increasing magnetic field at 14 K.

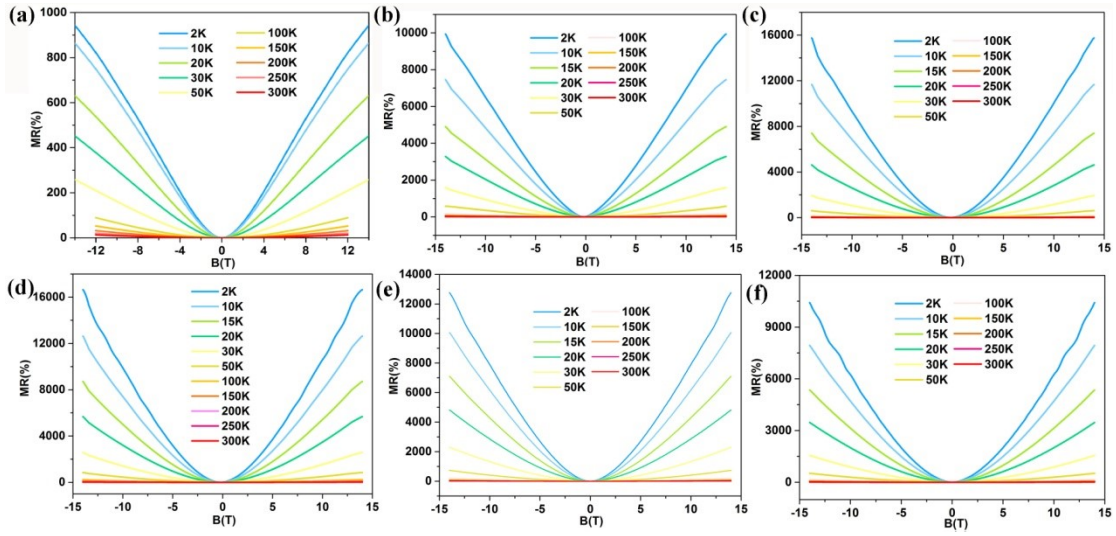

Fig. S5. The MR of $Mg_{3+\delta}Bi_2$:Mn_x with (a) x = 0, (b) x = 0.025, (c) x = 0.075, (d) x = 0.1, (e) x = 0.125, (f) x = 0.15 at different temperatures in a magnetic field between −14 and 14 Tesla.

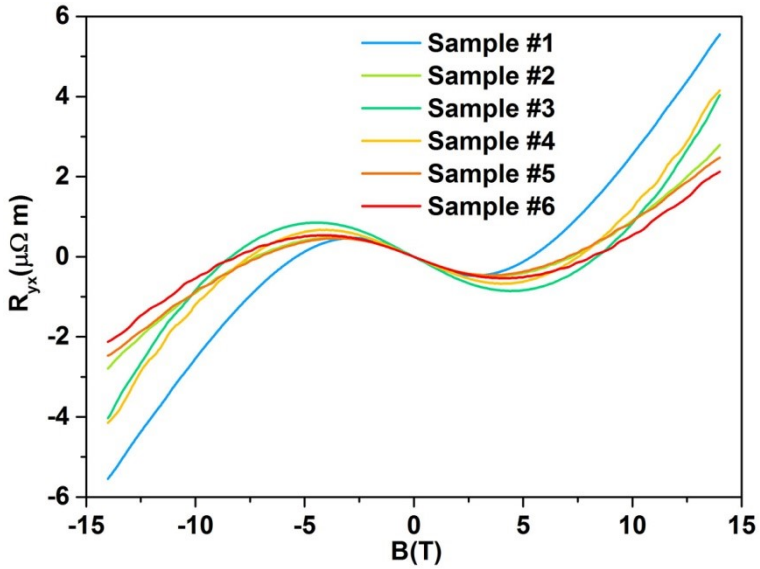

Fig. S6. The Hall resistivity ρ_{xy} of $Mg_{3+\delta}Bi_2$:Mn_x samples measured in the magnetic field range between -14 Tesla and 14 Tesla at 2 K.

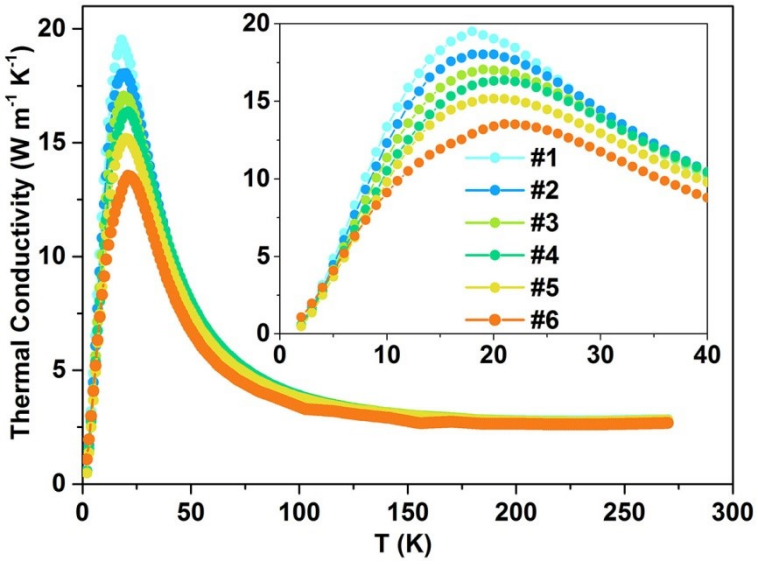

Fig. S7. The temperature-dependent thermal conductivity κ_{xx} of the as-fabricated $Mg_{3+\delta}Bi_2$:Mn_x series samples in the temperature range of 2 - 275 K. The peak κ_{xx} near 20 K was observed in all samples, which can be attributed to the phonon-phonon scattering process. With the increase of Mn content, the peak κ_{xx} gradually decreases from 19.49 $Wm^{-1}K^{-1}$ for sample #1 to 13.53 $Wm^{-1}K^{-1}$ for sample #6, suggesting that the introduction of Mn element brings the lattice defects and inhibits phonon transmission.

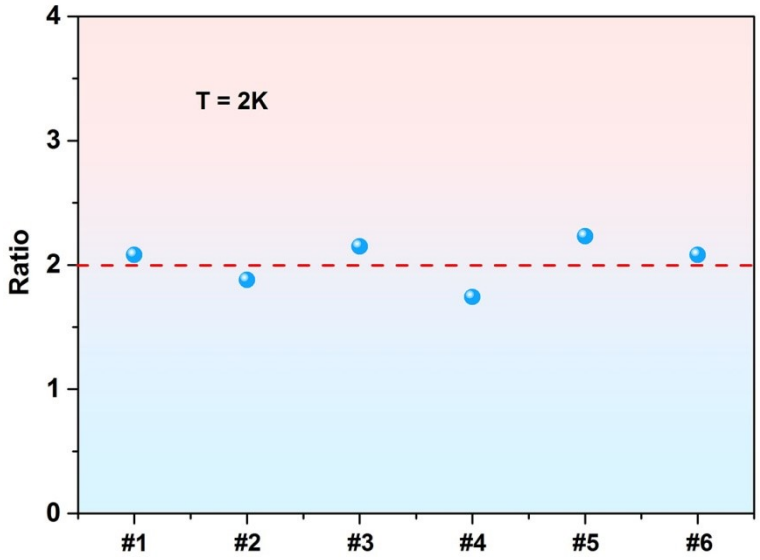

Fig. S8. The ratio of hole to electron concentration in the Mn-doped $Mg_{3+\delta}Bi_2$ samples at 2 K.

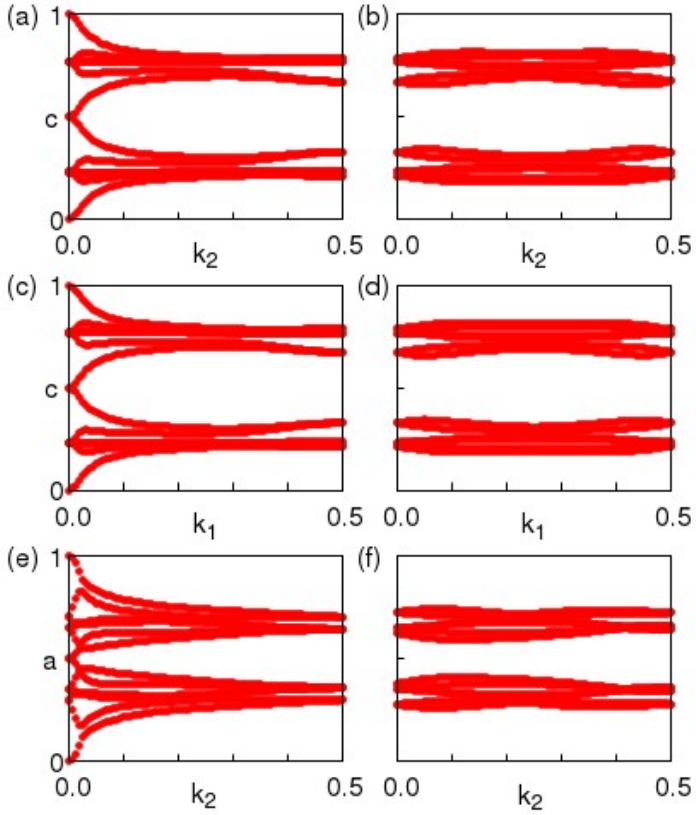

Fig. S9. Wannier charge center evolution for the 6 time reversal invariant $\vec{k}$ planes, i.e. (a) $k_1 = 0.0$, $Z_2 = 1$; (b) $k_1 = 0.5$, $Z_2 = 0$; (c) $k_2 = 0.0$, $Z_2 = 1$; (d) $k_2 = 0.5$, $Z_2 = 0$; (e) $k_3 = 0.0$, $Z_2 = 1$; (f) $k_3 = 0.5$, $Z_2 = 0$. So the bulk Z_2 topological number of pristine Mg_3Bi_2 is (1, 000), indicating its strong topological property.

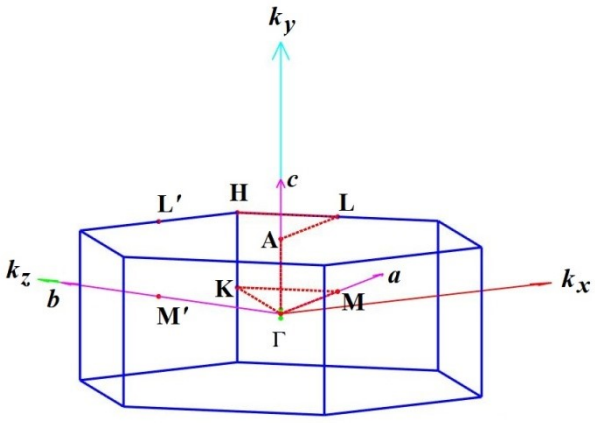

Fig. S10. The first Brillouin zone, high symmetric k points and the corresponding k-path (red dashed lines) for the band structure calculations. The two green dots along k_z direction are Dirac points.

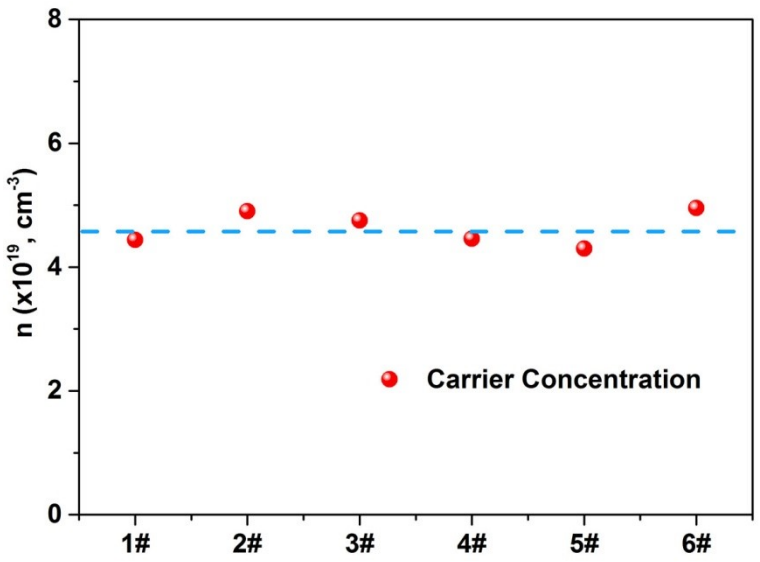

Fig. S11. The carrier concentrations of the obtained Mn-doped Mg_3Bi_2 samples at 300K.

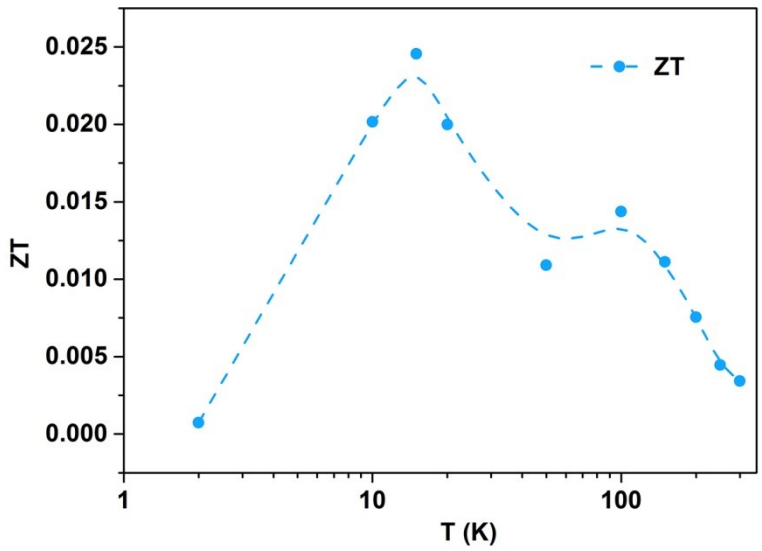

Fig. S12. ZT values of $Mg_{3+\delta}Bi_2$:$Mn_{0.1}$ sample in the temperature range between 2 K and 300 K.

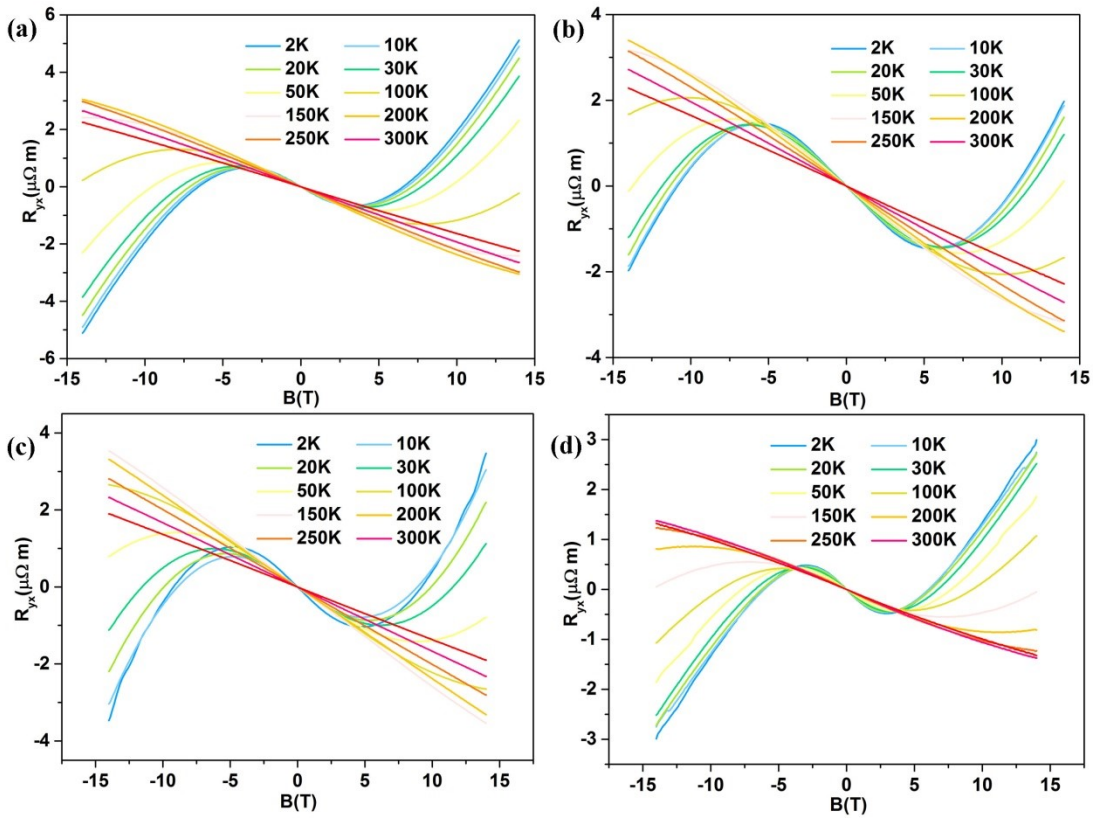

Fig. S13. Hall resistivity of (a) Nb, (b) Cr, (c) Fe, and (d) Co doped $Mg_{3+\delta}Bi_2$ materials in the magnetic field range between -14 Tesla and 14 Tesla.

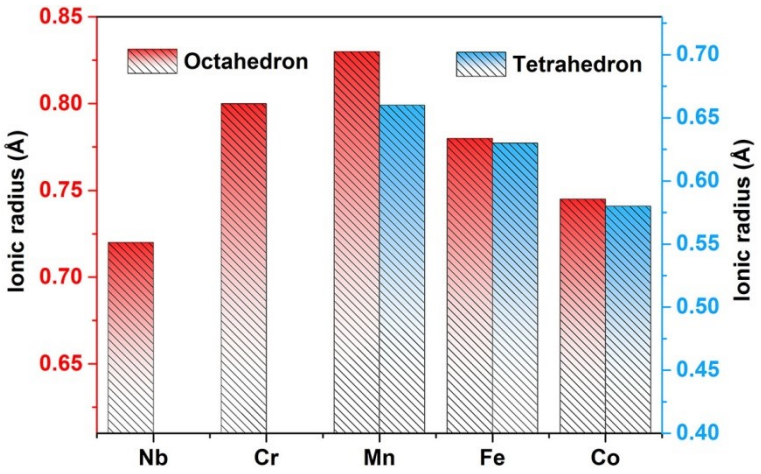

Fig. S14. The ionic radius of Nb, Cr, Mn, Fe, and Co, respectively. The red and blue represent the ionic radius of transition metal ions with four coordination and six coordination, respectively.

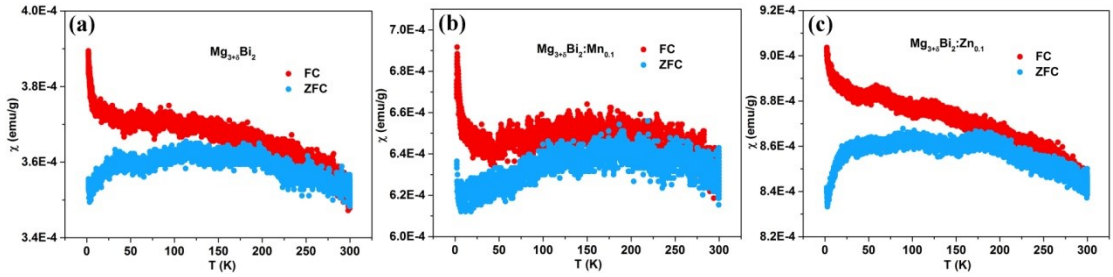

Fig. S15. M-T curves of $Mg_{3+\delta}Bi_2$, $Mg_{3+\delta}Bi_2:Zn_{0.1}$ and $Mg_{3+\delta}Bi_2:Mn_{0.1}$ samples measured at 500Oe between 2 K and 300 K.

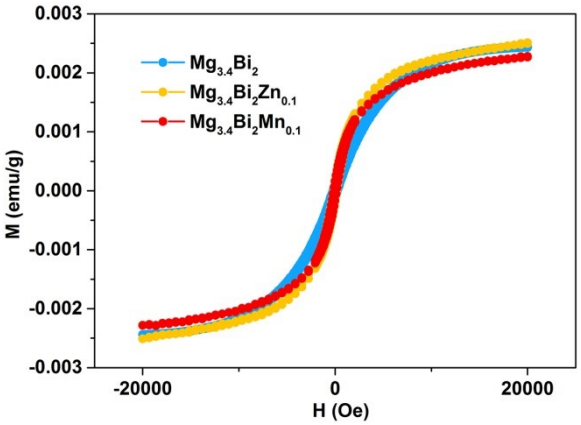

Fig. S16. M-H curves of $Mg_{3.4}Bi_2$, $Mg_{3.4}Bi_2Zn_{0.1}$, $Mg_{3.4}Bi_2Mn_{0.1}$ at 2 K between -20000 Oe and 20000 Oe.

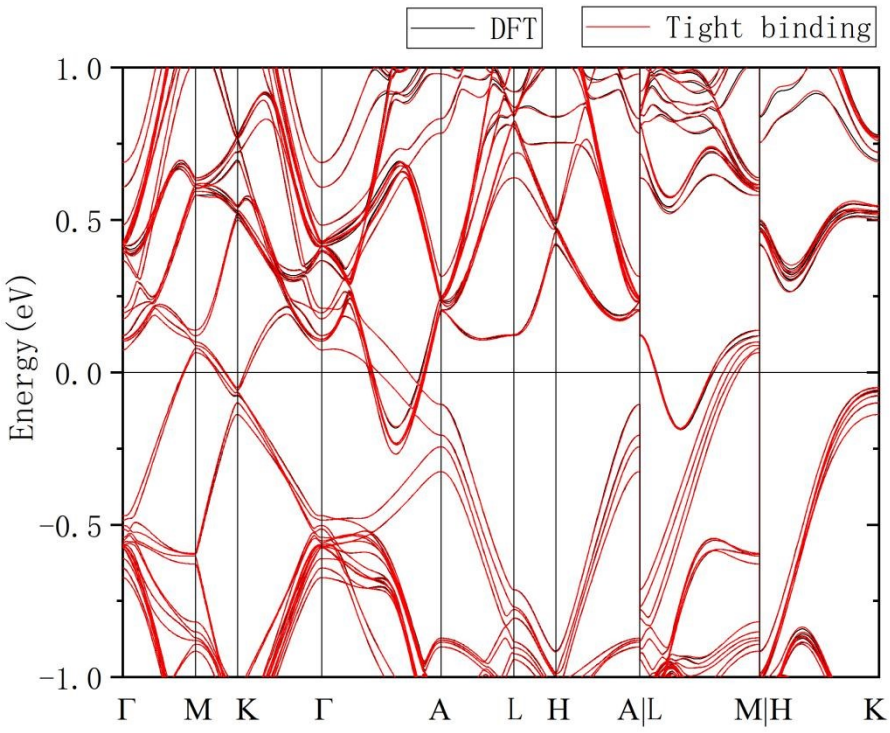

Fig. S17. DFT Calculated band structure (black line) and the fitted band structure with tight binding model (red line) implemented in Wannier90 package with SOC for Mn doping $Mg_{3+\delta}Bi_2$ for tetrahedral substitution with a $3 \times 3 \times 1$ supercell with 0.7% tensile strain. The effective band structure (Figure 3f in the main text) is obtained by unfolding this band structure. And the transport calculations (MR in Figures 4a-4b in the main text) are also based on this band structure.

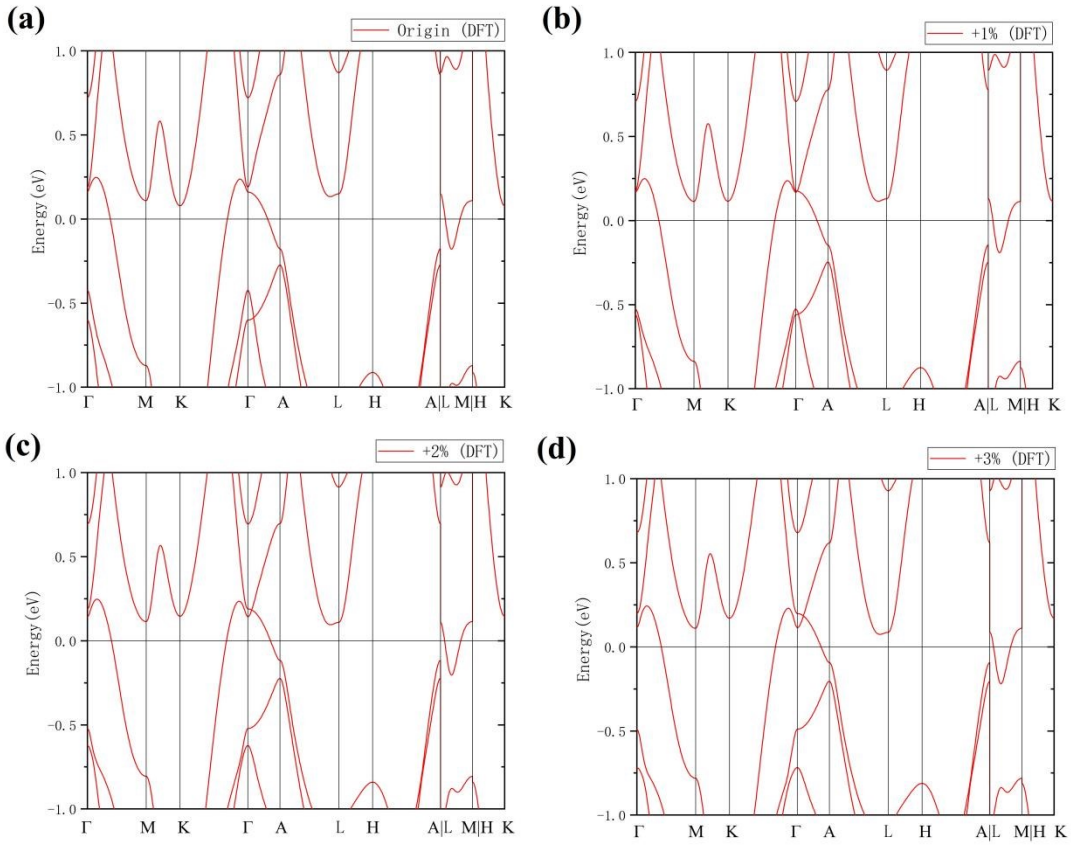

Fig. S18. Band structures of pristine Mg_3Bi_2 with various homogeneous tensile strains, i.e. (a) origin, (b) 1%, (c) 2% and (d) 3%. The Dirac point moves towards A point along the $\Gamma - A$ line with the increase of the tensile strain.

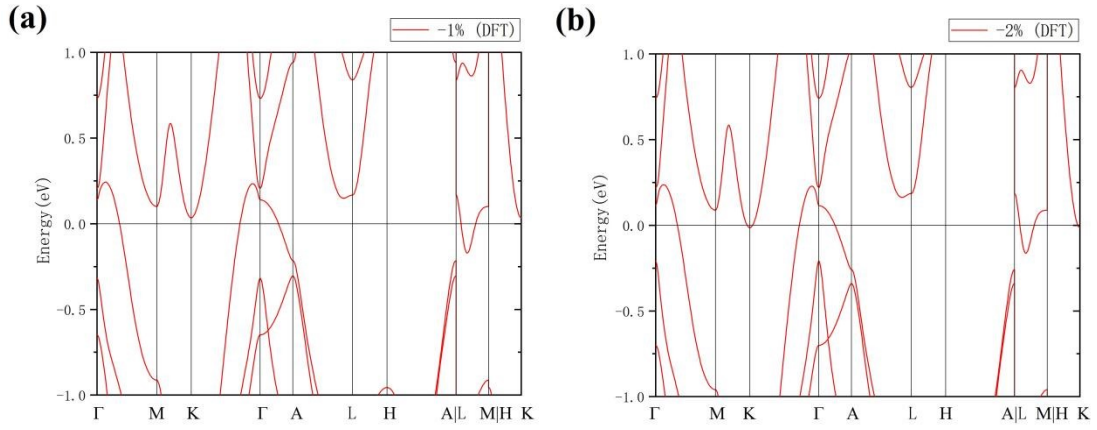

Fig. S19. Band structures of pristine Mg_3Bi_2 with compressive strain, i.e. (a) -1% and (b) -2%. The Z_2 topological gap increases with the compressive strain.

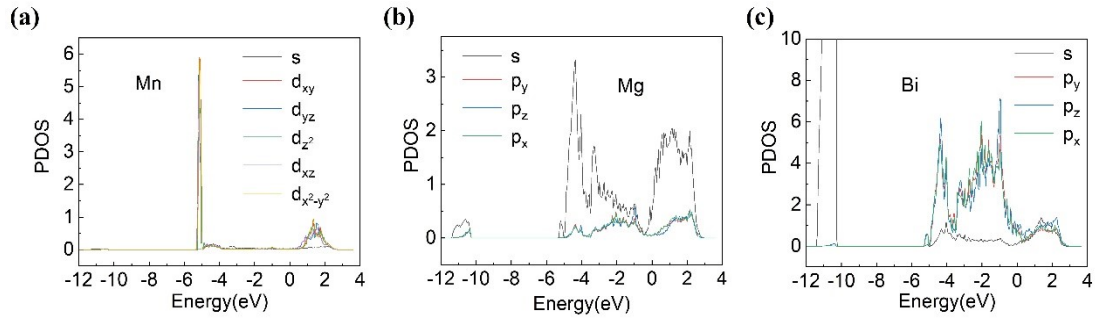

Fig. S20. PDOS of Mn doping Mg_3Bi_2 for each element, i.e., (a) Mn, (b) Mg, and (c) Bi. The occupied d orbitals of Mn locate in the deep energy level, more than 5 eV away from Fermi level. And the dominated components around the Fermi level are still Mg-s and Bi-p.

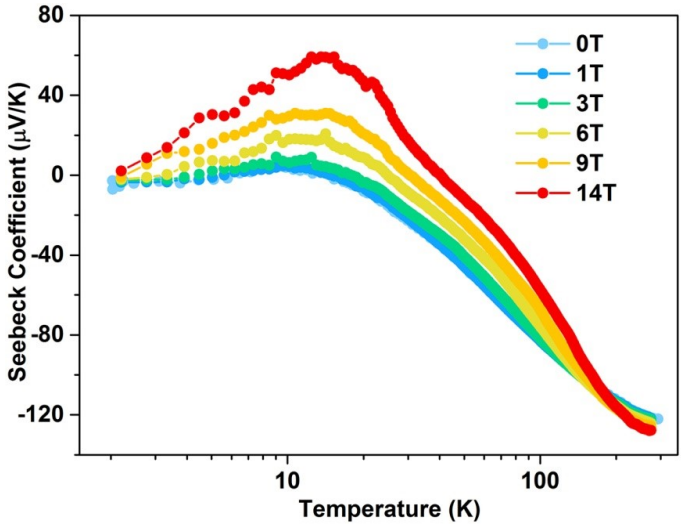

Fig. S21. Longitudinal Seebeck coefficient under different magnetic fields in a temperature range of 2-300 K.

Table S1. Nominal and actual components of the Mn-doped Mg_3Bi_2 series of samples.

Sample	Nominal components	Actual components
#1	$Mg_{3.4}Bi_2$	$Mg_{3.145}Bi_2$
#2	$Mg_{3.4}Bi_2$:$Mn_{0.025}$	$Mg_{3.101}Bi_2$:$Mn_{0.021}$
#3	$Mg_{3.4}Bi_2$:$Mn_{0.075}$	$Mg_{3.068}Bi_2$:$Mn_{0.066}$
#4	$Mg_{3.4}Bi_2$:$Mn_{0.1}$	$Mg_{3.054}Bi_2$:$Mn_{0.082}$
#5	$Mg_{3.4}Bi_2$:$Mn_{0.125}$	$Mg_{3.017}Bi_2$:$Mn_{0.120}$
#6	$Mg_{3.4}Bi_2$:$Mn_{0.15}$	$Mg_{2.907}Bi_2$:$Mn_{0.156}$

Table S2. Refined crystallographic parameters for $Mg_{3+\delta}Bi_2$:Mn_x (x = 0) with trigonal structure.

$Mg_{3+\delta}Bi_2$:Mn_x (x = 0)						
Atom	x	y	z	Mult	Occupancy	U_{iso}
Bi	0.3333	0.6667	0.2350	2	1.0000	0.0250
Mg1	0.0000	0.0000	0.0000	1	1.0000	0.0250
Mg2	0.3333	0.6667	0.6300	2	1.0000	0.0250

Table S3. Refined crystallographic parameters for $Mg_{3+\delta}Bi_2$:Mn_x (x = 0.025) with trigonal structure.

$Mg_{3+\delta}Bi_2$:Mn_x (x = 0.025)						
Atom	x	y	z	Mult	Occupancy	U_{iso}
Bi	0.3333	0.6667	0.2350	2	1.0000	0.0250
Mg1	0.0000	0.0000	0.0000	1	1.0000	0.0250
Mg2	0.3333	0.6667	0.6300	2	0.9875	0.0250
Mn2	0.3333	0.6667	0.6300	2	0.0125	0.0250

Table S4. Refined crystallographic parameters for $Mg_{3+\delta}Bi_2$:Mn_x (x = 0.075) with trigonal structure.

$Mg_{3+\delta}Bi_2$:Mn_x (x = 0.075)						
Atom	x	y	z	Mult	Occupancy	U_{iso}
Bi	0.3333	0.6667	0.2350	2	1.0000	0.0250
Mg1	0.0000	0.0000	0.0000	1	1.0000	0.0250
Mg2	0.3333	0.6667	0.6300	2	0.9625	0.0250
Mn2	0.3333	0.6667	0.6300	2	0.0375	0.0250

Table S5. Refined crystallographic parameters for $Mg_{3+\delta}Bi_2:Mn_x$ (x = 0.1) with trigonal structure.

$Mg_{3+\delta}Bi_2:Mn_x$ (x = 0.1)						
Atom	x	y	z	Mult	Occupancy	U_{iso}
Bi	0.3333	0.6667	0.2350	2	1.0000	0.0250
Mg1	0.0000	0.0000	0.0000	1	1.0000	0.0250
Mg2	0.3333	0.6667	0.6300	2	0.9500	0.0250
Mn2	0.3333	0.6667	0.6300	2	0.0500	0.0250

Table S6. Refined crystallographic parameters for $Mg_{3+\delta}Bi_2$:Mn_x (x = 0.125) with trigonal structure.

$Mg_{3+\delta}Bi_2$:Mn_x (x = 0.125)						
Atom	x	y	z	Mult	Occupancy	U_{iso}
Bi	0.3333	0.6667	0.2350	2	1.0000	0.0250
Mg1	0.0000	0.0000	0.0000	1	1.0000	0.0250
Mg2	0.3333	0.6667	0.6300	2	0.9375	0.0250
Mn2	0.3333	0.6667	0.6300	2	0.0625	0.0250

Table S7. Refined crystallographic parameters for $Mg_{3+\delta}Bi_2:Mn_x$ (x = 0.15) with trigonal structure.

$Mg_{3+\delta}Bi_2:Mn_x$ (x = 0.15)						
Atom	x	y	z	Mult	Occupancy	U_{iso}
Bi	0.3333	0.6667	0.2350	2	1.0000	0.0250
Mg1	0.0000	0.0000	0.0000	1	1.0000	0.0250
Mg2	0.3333	0.6667	0.6300	2	0.9275	0.0250
Mn2	0.3333	0.6667	0.6300	2	0.0725	0.0250

Supplementary References

1. Liechtenstein AI, Anisimov VI and Zaanen, Density-functional theory and strong interactions: Orbital ordering in Mott-Hubbard insulators. *J Phys Rev B* 1995; **52**: R5467-70.

2. Kresse G and Furthmüller. Efficiency of ab-initio total energy calculations for metals and semiconductors using a plane-wave basis set. *J Comput Mater Sci* 1996; **6**: 15.

3. Kresse G and Furthmüller, Efficient iterative schemes for ab initio total-energy calculations using a plane-wave basis set. J. *Phys Rev B* 1996; **54**: 11169.

4. Perdew JP, Burke K and Ernzerhot M *et al*. Generalized Gradient Approximation Made Simple. *Phys Rev Lett* 1996; **77**: 3865.

5. Blöchl PE. Projector augmented-wave method. *Phys Rev B* 1994; **50**: 17953.

6. Kresse G and Joubert D. From ultrasoft pseudopotentials to the projector augmented-wave method. *Phys Rev B* **59**, 1758 (1999).

7. Zhang SN, Wu QS and Liu Y *et al*. Magnetoresistance from Fermi surface topology. *Phys Rev B* 2019; **99**: 035142.

8. Liu Y, Zhang HJ and Yao YG. Ab initio investigation of magnetic transport properties by Wannier interpolation. *Phys Rev B* 2009; **79**: 245123.

9. Mostofifi AA, Yates JR and Pizzi G *et al.* An updated version of wannier90: A tool for obtaining maximally-localised Wannier functions. *Comput. Phys Commun* 2014; **185**: 2309.

10. Marzari N and Vanderbilt D. Maximally localized generalized Wannier functions for composite energy bands. *Phys Rev B* 1997; **56**: 12847.

11. Souza I, Marzari N and Vanderbilt D. Maximally localized Wannier functions for entangled energy bands. *Phys Rev B* 2001; **65**: 035109.

12. Marzari N, Mostofifi AA and Yates JR *et al.* Maximally localized Wannier functions: Theory and applications. *Rev Mod Phys* 2012; **84**: 1419.

13. Gao JC, Wu Q and Persson C *et al*. Irvsp: to obtain irreducible representations of electronic states in the VASP. *Comput. Phys Commun* 2021; **261**: 107760.